

A Halo Model Approach to the 21 cm and Ly α Cross-correlation

Chang Feng*,¹ Asantha Cooray,¹ and Brian Keating²

¹*Department of Physics and Astronomy, University of California, Irvine, CA 92697, USA*

²*Department of Physics, University of California, San Diego, CA 92093, USA*

We present a halo-model-based approach to calculate the cross-correlation between 21 cm HI intensity fluctuations and Ly α emitters (LAE) during the epoch of reionization (EoR). Ionizing radiation around dark matter halos are modeled as bubbles with the size and growth determined based on the reionization photon production, among other physical parameters. The cross-correlation shows a clear negative-to-positive transition, associated with transition from ionized to neutral hydrogen in the intergalactic medium during EoR. The cross-correlation is subject to several foreground contaminants, including foreground radio point sources important for 21 cm experiments and low- z interloper emission lines, such as H α , OIII, and OII, for Ly α experiments. Our calculations show that by masking out high fluxes in the Ly α measurement, the correlated foreground contamination on the 21 cm–Ly α cross-correlation can be dramatically reduced. We forecast the detectability of 21 cm–Ly α cross-correlation at different redshifts and adopt a Fisher matrix approach to estimate uncertainties on the key EoR parameters that have not been well constrained by other observations of reionization. This halo-model-based approach enables us to explore the EoR parameter space rapidly for different 21 cm and Ly α experiments.

PACS numbers:

I. INTRODUCTION

The early universe, initially filled with hot plasma, became neutral as hydrogen ions captured electrons that were decoupled from cosmic microwave background (CMB) photons at a redshift of 1100. A cosmic “dark age” subsequently ensued in the universe until the linear density fluctuations seeded by inflation were amplified, forming the first stars and galaxies [1]. The X-rays from mini quasars and ultraviolet radiation from the massive stars in first-light galaxies heated and ionized the neutral hydrogen, and the universe gradually transformed from completely neutral to fully ionized during the epoch of reionization (EoR). Today the EoR still remains largely unexplored, as signatures imprinted on the intergalactic medium (IGM) in the early universe are too faint to be detected.

The physical processes present during the EoR are of extreme importance to our understanding of the universe and the structure that formed in it. The clustering of neutral hydrogen (HI) down to the Jeans length scale contains a wealth of information about certain fundamental physics, including dark matter. The HI tomography is not subject to small-scale physical effects such as photon diffusion damping present in the CMB power spectrum. The timing and duration of the EoR can help interpret other cosmological measurements, such as the kinetic Sunyaev-Zel’dovich (kSZ) effect [2]. Moreover, some exotic physics such as primordial magnetic fields [3] and decaying dark matter [4] could be probed during the EoR. To date, the neutral fraction during the EoR was measured from quasar absorption spectra [5] and Ly α -

emitting galaxy luminosity functions [6–8] around $z \sim 6$. Another important quantity of the EoR, the Thomson scattering optical depth, is constrained to $\tau = 0.088 \pm 0.014$ by WMAP [9] and $\tau = 0.058 \pm 0.012$ by Planck satellites [10].

The best way to measure the HI content prior to and during reionization is through the 21 cm HI fine-structure spin-flip transition. A number of experiments have been targeting the 21 cm emission, such as the Low Frequency Array (LOFAR) [11], the Murchison Widefield Array (MWA) [12], the Precision Array for Probing the Epoch of Reionization (PAPER) [13], the Hydrogen Epoch of Reionization Array (HERA) [14] and the Square Kilometer Array (SKA) [15]. The redshifted 21 cm emission is contaminated by both galactic and extragalactic foregrounds that consist of galactic synchrotron, supernovae remnants, free-free emission, and radio point sources [16]. The Galactic synchrotron emission is the dominant contribution, as it is three to four orders of magnitude stronger than the background brightness temperature fluctuations. By performing a component separation or subtracting the 21 cm foreground, the 21 cm brightness fluctuations could be measured [17]. This, however, relies on the reliability of the foreground estimation. The radio point sources are also thought to be another foreground issue for 21 cm experiments, but this signal is very likely to be a subdominant contamination [18]. The expected 21 cm signal is at the level of 10 mK^2 at $k = 0.3 \text{ Mpc}^{-1}$ [19], while recent measurements from PAPER set a 2σ upper limit as $(22.4 \text{ mK})^2$ in the range $0.15 < k < 0.5 \text{ h Mpc}^{-1}$ at $z = 8.4$ [20].

During the EoR the ultraviolet Ly α emission was created by the first stars and galaxies. The Ly α background traces the underlying dark matter distribution and also affects the spin-temperature distribution. By directly measuring the Ly α emissions, we get an additional ob-

*chang.feng@uci.edu

servable on EoR physics as well [21]. However, the Ly α background is contaminated by low- z foregrounds, such as H α at $z = 0.5$, OIII at $z = 0.9$, and OII at $z = 1.6$. These low- z components are much brighter than Ly α , precluding a clean detection. On the other hand, such low- z foregrounds can be easily masked out since they are very bright [22, 23]. Therefore, a simple masking procedure would recover the genuine Ly α background from experiments.

The 21 cm and Ly α emission is anti-correlated at large angular scales because they originate from IGM and galaxies, respectively, and ionized bubbles around Ly α galaxies are devoid of HI that is seen with 21 cm experiments. The transition in the cross-correlation from negative to positive indicates a characteristic size for the average of HII regions around halos. Therefore, the cross-correlation between 21 cm and Ly α can be viewed as a complementary probe of EoR physics. The cross-correlation could be more advantageous in terms of foreground removal as the two sets of aforementioned foregrounds would be largely uncorrelated, potentially allowing a higher signal-to-noise detection and an easy confirmation of the EoR signature. Previously, the cross-correlation between 21 cm experiments and galaxies was studied for 21 cm experiments such as MWA and LOFAR, using both analytical and numerical calculations [24–26], as well as for LOFAR and Subaru’s Hyper Suprime-cam [27]. The cross-correlation between 21 cm and CO/kSZ also shows a similar transition in the correlation sign [28, 29].

So far, different approaches have been used to model reionization. The large-scale N -body and radiative transfer simulations, while desirable, are challenging because it is computationally intensive due to the large dynamic range [30, 31]. Another approach involves semi-analytical/semi-numerical models by taking a halo catalog generated from N -body simulations and generating a reionization field by smoothly filtering the halo field [32, 33]. A more simplified idea of this semi-numerical simulation is to make the density field from Gaussian random variables instead of relying on the N -body simulations. The simulation can be done efficiently within a small box for EoR [19, 34]. However, this numerical solution becomes ineffective when the box is too large or the simulated epoch is far beyond the EoR when the CMB temperature T_{cmb} is coupled to the spin temperature T_s and the assumption $T_s \gg T_{\text{cmb}}$ breaks down. An upgraded version of this implementation uses a very similar algorithm to extend to large boxes [35]. Here, we apply a very simple ionizing bubble model [36] to the calculations of 21 cm brightness temperature anisotropy and its cross-correlation with Ly α analytically, so we can quickly forecast the detectability of the signal for different combinations of 21 cm and Ly α experiments, and explore the EoR parameter space without significant computational cost. This approach would be very beneficial when the cross-correlation measurements with different experiments and major foreground or instrumental issues

need to be identified in the early stage of the development.

This paper is organized as follows. In Section II, we introduce the halo model for the ionizing bubble as well as the cross-correlation. In Section III, the Ly α luminosity is discussed. Then we focus on the low- z foregrounds for both 21 cm and Ly α measurements in Section IV and estimate signal-to-noise for the detectability of different experiments, as well as the uncertainties on the EoR parameters in Section V. We conclude in Section VI. We use the Planck cosmological parameters: $\Omega_b h^2 = 0.02230$, $\Omega_c h^2 = 0.1188$, $H_0 = 67.74$ km/s/Mpc, $Y_p = 0.249$, $\ln(10^{10} A_s) = 3.064$ at $k_* = 0.05$ Mpc $^{-1}$, $n_s = 0.9667$, and $\tau = 0.058$.

II. THEORETICAL MODEL OF THE CROSS-CORRELATION

Here we describe the basic ingredients of our halo model. Since the mean ionizing fraction is not precisely constrained by current observations, we use the CAMB’s reionization model [37]; i.e.,

$$\bar{x}_e(z) = \frac{1}{2} \left[1 + \tanh \left(\frac{(1 + z_{\text{re}})^{3/2} - (1 + z)^{3/2}}{\Delta y} \right) \right], \quad (1)$$

where the redshift z_{re} is derived from the optical depth τ today; i.e.,

$$\tau = \int_0^{\chi_{\text{re}}} dl n_e(\chi') \sigma_T, \quad (2)$$

and $\Delta y = 1.5\sqrt{1 + z_{\text{re}}}\Delta z$. Here, σ_T is the Thomson cross-section, the electron density is $n_e = (1 - 3/4Y_p)\rho_{b,0}/m_H a^{-3} x_e$, the comoving length $dl = ad\chi'$, the Helium fraction is Y_p , the proton mass is m_H , and the mean neutral hydrogen fraction is $\bar{x}_H = 1 - \bar{x}_e$. We assume that helium is singly ionized along with hydrogen, while the double ionization of helium is neglected.

The 21 cm brightness temperature can be split into two components, $T_0(z)\psi(\mathbf{x}, z)$, in which the isotropic background temperature is

$$T_0(z) = 27 \left(\frac{1 - Y_p}{1 - 0.248} \right) \left(\frac{\Omega_b}{0.044} \right) \left[\left(\frac{0.27}{\Omega_m} \right) \left(\frac{1 + z}{10} \right) \right]^{1/2} \text{ (mK)}, \quad (3)$$

and spatial fluctuation ψ is [38]

$$\psi(\mathbf{x}, z) = \bar{x}_H(1 + \delta_x)(1 + \delta) = \bar{x}_H(1 + \delta_x + \delta + \delta_x\delta). \quad (4)$$

Here δ_x is the density contrast of ionizing field (x) and we neglect perturbations introduced by spin-temperature fluctuations and peculiar velocities. For the 21 cm field, we only consider the signals from IGM as galaxy contributions are 10^{-4} times smaller [39], and model the ionizing field with “bubbles” [38]. From Eq. (4), the two-point correlation functions for ionizing and matter density contrasts are $\langle \delta_x \delta_x \rangle = \xi_{xx}/\bar{x}_H^2$, $\langle \delta_x \delta \rangle = \xi_{x\delta}/\bar{x}_H$, and $\langle \delta \delta \rangle = \xi_{\delta\delta}$.

The auto-correlation function of the isotropic 21 cm spatial fluctuation field is [40, 41]

$$\xi_{\psi\psi} = \xi_{xx}(1 + \xi_{\delta\delta}) + \bar{x}_H^2 \xi_{\delta\delta} + \xi_{x\delta}(2\bar{x}_H + \xi_{x\delta}) + \xi_{x\delta x\delta}. \quad (5)$$

We should note that this 21 cm auto-correlation function is only an approximation in that the three-point correlation terms neglected are generally substantial, as [42] pointed out. However, we mainly focused on the cross-correlation calculations, for which we did consider all of the higher order terms. Although the assumption that the density field is Gaussian is a reasonable approximation on most of the scales of interest, we create the ionizing field from a Poisson process, as we will discuss later, to account for its non-Gaussianity. We only use power spectrum to do the statistics so that the non-Gaussianity of the field is not captured [40]. We neglect the redshift distortions and make use of the fact that the spin temperature is significantly higher than CMB at $z < 10$ [43]. We Fourier transform the correlation function, assuming that the quadratic terms are negligibly small. The 21 cm power spectrum is

$$\begin{aligned} P_{\psi\psi}^{(2h)} &= P_{xx}^{(2h)} + \bar{x}_H^2 P_{\delta\delta}^{(2h)} + 2\bar{x}_H P_{x\delta}^{(2h)} + P_{x\delta x\delta}^{(2h)} \\ &\simeq P_{xx}^{(2h)} + \bar{x}_H^2 P_{\delta\delta}^{(2h)} + 2\bar{x}_H P_{x\delta}^{(2h)}. \end{aligned} \quad (6)$$

The power spectrum can be calculated from a halo model by describing HII regions as bubbles. The two-halo term of $P_{x\delta x\delta}$ is higher order and negligible [41].

The virial temperature of halo $T_{\text{vir}} = 5 \times 10^4$ K (suggested by [38]) sets the minimum halo mass

$$\frac{T_{\text{vir}}}{10^4 \text{K}} = 1.1 \left(\frac{\Omega_m h^2}{0.15} \right)^{1/3} \left(\frac{1+z}{10} \right) \left(\frac{M_{\text{th}}}{10^8 M_\odot} \right)^{2/3}. \quad (7)$$

With this threshold mass, we can calculate the mean number density of bubble $\bar{n}_b = \int_{M_{\text{th}}}^\infty dM \frac{dn}{dM}$ and the average bubble size from $\bar{n}_b = -(\ln \bar{x}_H)/\bar{V}_b$. When it is compared to the predicted value

$$\bar{V}_b = \int dR P(R) V_b(R) = \frac{4\pi \bar{R}^3}{3} e^{9\sigma_{\ln R}^2}, \quad (8)$$

the bubble radius is constrained. The bubble radius R is assumed to satisfy a logarithmic distribution [25] as

$$P(R) = \frac{1}{R} \frac{1}{\sqrt{2\pi\sigma_{\ln R}^2}} e^{-\frac{1}{2} \left(\frac{\ln(R/\bar{R})}{\sigma_{\ln R}} \right)^2}. \quad (9)$$

In Figure 1, we show the distribution of the bubble size at different redshifts.

Given the average volume and number density, the ionizing field is generated from a Poisson process

$$\langle x_e(\mathbf{x}) \rangle = 1 - e^{-n_b(\mathbf{x})\bar{V}_b}, \quad (10)$$

and its number density is

$$n_b(\mathbf{x}) = \bar{n}_b(1 + b\delta_L(\mathbf{x})), \quad (11)$$

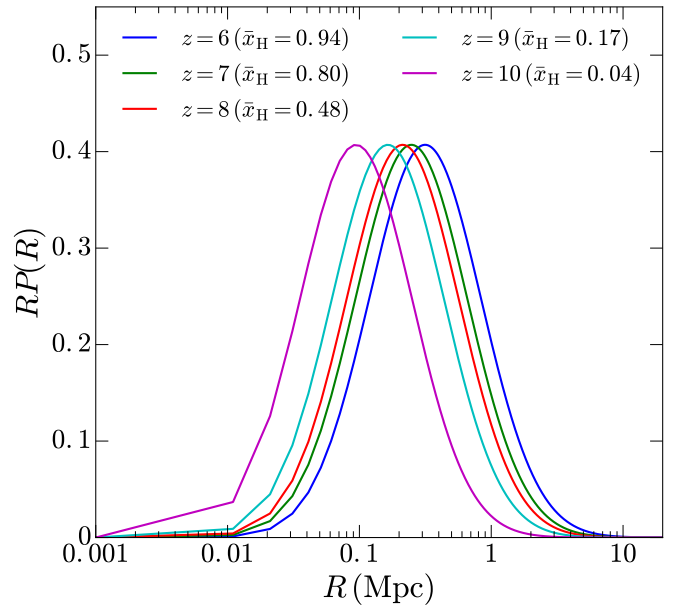


FIG. 1: Bubble size radius R is assumed to satisfy a logarithmic distribution in Eq. (9). We show the distributions at redshifts $z = 6, 7, 8, 9,$ and 10 . The mean ionization fractions \bar{x}_H at these redshifts are given in parentheses.

where the density contrast δ_L is the matter density δ smoothed by a top-hat window of radius R . The top-hat window in Fourier space is

$$\bar{W}_R^n(k) = \frac{1}{\bar{V}_b^n} \int_0^\infty dR P(R) [V_b(R) W(kR)]^n. \quad (12)$$

The shape factor for the ionizing field x is defined as

$$X_l^{(x)}(k, M, z) = \bar{x}_H \ln \bar{x}_H b_{\text{bubble}} \bar{W}_R(k) u_1, \quad (13)$$

with the bubble bias given by

$$b_{\text{bubble}} = \frac{1}{\bar{n}_b} \int_{M_{\text{th}}}^\infty b(M, z) \frac{dn}{d \ln M} \frac{dM}{M}. \quad (14)$$

Here, u_1 is the Fourier transform of the NFW profile [44]; i.e., $u_1 = M/\bar{\rho}_m u$. The NFW Fourier transform is

$$u(k, M, z) = \frac{1}{M} \int_0^{r_{\text{vir}}} dr 4\pi r^2 \frac{\sin kr}{kr} \rho_{\text{NFW}}, \quad (15)$$

which is derived from a standard NFW profile

$$\rho_{\text{NFW}} = \rho_s \left(\frac{r}{r_s} \right)^{-1} \left(1 + \frac{r}{r_s} \right)^{-2}. \quad (16)$$

The detailed discussions of ρ_s , r_s and r_{vir} can be found in Ref. [45].

The 1-halo term of the 21 cm field [46, 47] is

$$\begin{aligned} P_{\psi\psi}^{(1h)} &= P_{xx}^{(1h)} + \bar{x}_H^2 P_{\delta\delta}^{(1h)} + 2\bar{x}_H P_{x\delta}^{(1h)} + P_{x\delta x\delta}^{(1h)} \\ &\simeq P_{xx}^{(1h)} + \bar{x}_H^2 P_{\delta\delta}^{(1h)} + P_{x\delta x\delta}^{(1h)}, \end{aligned} \quad (17)$$

where $P_{xx}^{(1h)} = (\bar{x}_e - \bar{x}_e^2)V_b\bar{W}_R^2$ and $P_{x\delta x\delta}^{(1h)} = (\bar{x}_e - \bar{x}_e^2)\tilde{P}_{\delta\delta}$. The term $P_{x\delta}^{(1h)}$ is zero as we assume the bubble is completely ionized. Here $\sigma_R^2 = \int dk k^2 / 2\pi^2 \bar{W}_R^2(k) P_{\delta\delta}(k)$ and $\tilde{P}_{\delta\delta} = P_{\delta\delta} V_b \sigma_R^2 / \sqrt{P_{\delta\delta}^2 + (V_b \sigma_R^2)^2}$. The two-halo term can be easily calculated with the shape factor in Eq. (13).

On the other hand, the intensity mapping (IM) of Ly α emitters (LAEs) is a biased tracer of the same dark matter distribution, i.e., $\sim (1 + \delta_\eta)$. For simplicity, we use $\delta_{\text{Ly}\alpha} = \delta_\eta$. The cross-correlation between 21 cm and LAEs is

$$\xi_{\psi\eta} = \bar{x}_H(\xi_{\delta_\eta\delta} + \xi_{\delta_\eta x\delta}) + \xi_{x\delta_\eta}, \quad (18)$$

and the 3D power spectrum is

$$P_{\psi\eta} = \bar{x}_H(P_{\delta_\eta\delta} + P_{\delta_\eta x\delta}) + P_{x\delta_\eta}. \quad (19)$$

Here, the two-halo and one-halo terms are given by

$$\begin{aligned} P_{\psi\eta}^{(2h)} &= \bar{x}_H(P_{\delta_\eta\delta}^{(2h)} + P_{\delta_\eta x\delta}^{(2h)}) + P_{x\delta_\eta}^{(2h)} \\ &\simeq \bar{x}_H P_{\delta_\eta\delta}^{(2h)} + P_{x\delta_\eta}^{(2h)} \end{aligned} \quad (20)$$

and

$$\begin{aligned} P_{\psi\eta}^{(1h)} &= \bar{x}_H(P_{\delta_\eta\delta}^{(1h)} + P_{\delta_\eta x\delta}^{(1h)}) + P_{x\delta_\eta}^{(1h)} \\ &\simeq 0, \end{aligned} \quad (21)$$

respectively. The subscript $\delta_\eta x\delta$ essentially refers to $\delta_\eta, x\delta$ and the “,” is omitted for simplicity.

On small scales $P_{\delta_\eta x\delta}^{1h}$ cancels out the term $P_{\delta_\eta\delta}^{1h}$, so the summation is almost zero [25]. Also, the large-scale information of $P_{\delta_\eta x\delta}^{2h}$ should be very negligible. With all of these approximations, the final power spectrum of the 21 cm–Ly α cross-correlation is

$$P_{\psi\eta} \simeq P_{x\delta_\eta}^{(2h)} + \bar{x}_H P_{\delta_\eta\delta}^{(2h)}. \quad (22)$$

The halo-model approach, i.e.,

$$P^{1h,XY}(k, z) = \int dM \frac{dn}{dM} X_l(k, M, z) Y_l(k, M, z) \quad (23)$$

and

$$\begin{aligned} P^{2h,XY}(k, z) &= P_{\text{lin}}(k, z) \int dM \frac{dn}{dM} b(M, z) \tilde{X}_l(k, M, z) \\ &\quad \times \int dM \frac{dn}{dM} b(M, z) \tilde{Y}_l(k, M, z), \end{aligned} \quad (24)$$

can be used to calculate each power spectrum in Eq. (22). In these equations, dn/dM is the mass function and $b(M, z)$ is the bias. The linear matter power spectrum is P_{lin} . We will work out the shape factors $X_l(k, M, z)$ and $Y_l(k, M, z)$ (or $\tilde{X}_l(k, M, z)$ and $\tilde{Y}_l(k, M, z)$) for Ly α in the next section.

III. Ly α EMISSION

The UV radiation emitted from massive and short-lived stars can ionize the neutral hydrogen in the interstellar medium (ISM) in galaxies and the number of ionizing photons closely depends on the star formation rate (SFR). In this work we consider an SFR model that is consistent with numerical simulations. The fitted SFR [48] is

$$\begin{aligned} \frac{\text{SFR}(M, z)}{M_\odot \text{yr}^{-1}} &= 2.8 \times 10^{-28} M^a \left(1 + \frac{M}{M_1}\right)^b \\ &\quad \times \left(1 + \frac{M}{M_2}\right)^d, \end{aligned} \quad (25)$$

where $a = 2.8$, $b = -0.94$, $d = -1.7$, $M_1 = 10^9 M_\odot$, and $M_2 = 7 \times 10^{10} M_\odot$.

The ionizing photons could escape the galaxies with a fraction $f_{\text{esc}}(M, z) = e^{-\alpha(M/M_\odot)^\beta}$, but the remains will ionize the hydrogen and 66% of the ionization will result in a recombination process that produces Ly α photons. The dust in the ISM can also absorb the Ly α emissions, and the remaining fraction that survives the dust extinction is $f_{\text{Ly}\alpha}(z)$. The luminosity due to the recombination is then calculated as

$$L_{\text{rec}}^{\text{GAL}}(M, z) = 1.55 \times 10^{42} (1 - f_{\text{esc}}) f_{\text{Ly}\alpha} \frac{\text{SFR}}{M_\odot \text{yr}^{-1}} \text{ (erg s}^{-1}\text{)}. \quad (26)$$

The ionizing radiation can heat the gas so that the process of hydrogen excitation and cooling produces Ly α emission as well. The luminosities due to excitation and cooling are

$$L_{\text{exc}}^{\text{GAL}}(M, z) = 4.03 \times 10^{41} (1 - f_{\text{esc}}) f_{\text{Ly}\alpha} \frac{\text{SFR}}{M_\odot \text{yr}^{-1}} \text{ (erg s}^{-1}\text{)}, \quad (27)$$

and

$$\begin{aligned} L_{\text{cooling}}^{\text{GAL}}(M, z) &= 1.69 \times 10^{35} f_{\text{Ly}\alpha} \left(1 + \frac{M}{10^8}\right) \\ &\quad \times \left(1 + \frac{M}{2 \times 10^{10}}\right)^{2.1} \left(1 + \frac{M}{3 \times 10^{11}}\right)^{-3} \text{ (erg s}^{-1}\text{)}, \end{aligned} \quad (28)$$

respectively.

Besides these line emissions, the continuum produces Ly α photons through stellar radiation, free-free (ff), free-bound (fb), and two-photon (2γ) processes. Among these contributions, the stellar emission with a blackbody spectrum below the Lyman limit is dominant and its luminosity is

$$L_{\text{stellar}}^{\text{GAL}}(M, z) = 5.12 \times 10^{40} f_{\text{Ly}\alpha} \frac{\text{SFR}}{M_\odot \text{yr}^{-1}} \text{ (erg s}^{-1}\text{)}. \quad (29)$$

Our calculation takes all of these continuum lines into account, and the detailed line luminosity can be found in Ref. [48].

The total Ly α luminosity $L(M, z)$ from a galaxy is a summation of all of the above components and the shape factor for Ly α field is

$$X_l(k, M, z) = \frac{L(M, z)}{4\pi D_L^2} y D_A^2 u(k, M, z). \quad (30)$$

Here the conversion factor from frequency to comoving distance is $y = d\chi/d\nu = \lambda/(ca^2)d\chi/dz$, λ is the line rest frame wavelength, and D_L and D_A are luminosity and angular comoving distances, respectively.

This construction of shape factor is only a mathematical definition that facilitates the halo-model calculations in Eqs. (23) and (24). We should note that for individual point-like Ly α emitters, it would appear to be extended due to spatial diffusion of Ly α photons [49, 50]. Also, the scattering of photons on the red-side of Ly α in the IGM would further damp the Ly α flux along the line of sight [51]. We first consider that the Ly α emission is a biased tracer of the underlying dark matter distribution and phenomenologically account for the extended structure by the mass- and redshift-dependent quantity $b(M, z)$ in Eq. (24) and the luminosity function $L(M, z)$. Next we will discuss some dominating effects of IGM on the Ly α emissions, but effects such as the damping wing of Ly α have to rely on a numerical simulation.

The mean Ly α intensity varies at different redshifts as

$$\bar{I}_{\text{Ly}\alpha}(z) = \int_{M_{\min}}^{M_{\max}} dM \frac{dn}{dM} \frac{L(M, z)}{4\pi D_L^2} y D_A^2, \quad (31)$$

where $M_{\min} = 10^8 M_\odot$ and $M_{\max} = 10^{13} M_\odot$.

The escaped photons from galaxies can ionize the IGM, which can also emit Ly α photons due to the recombination process. The recombination rate is

$$\dot{n}_{\text{rec}} = \alpha n_e n_{\text{HII}}, \quad (32)$$

where $n_e = x_e n_b$, $n_{\text{HII}} = x_e n_b C$, $C = (1 - Y_p)/(1 - 3Y_p/4)$, and α is a case A comoving recombination coefficient. The luminosity function of IGM is $L_{\text{rec}}^{\text{IGM}} = f_{\text{rec}} \dot{n}_{\text{rec}} E_{\text{Ly}\alpha}$ and the fraction f_{rec} is spin-temperature dependent. We show the contribution of IGM in Figure 2 and it is seen that the IGM contribution is negligible for both auto- and cross-power spectra.

Another IGM contribution to Ly α emission comes from the scattering of Ly n photons escaping from galaxies. From the previous calculations [22, 48, 52], it is found that the diffuse IGM contribution is a few orders of magnitude smaller than the galaxies. Therefore, we ignore this contribution to the overall Ly α signal.

IV. LOW-Z FOREGROUNDS

The Ly α emission at the EoR can be significantly contaminated by low- z foregrounds. The foreground at z_f projected onto the source plane z_s becomes anisotropic as the wave vector of the foreground power spectrum

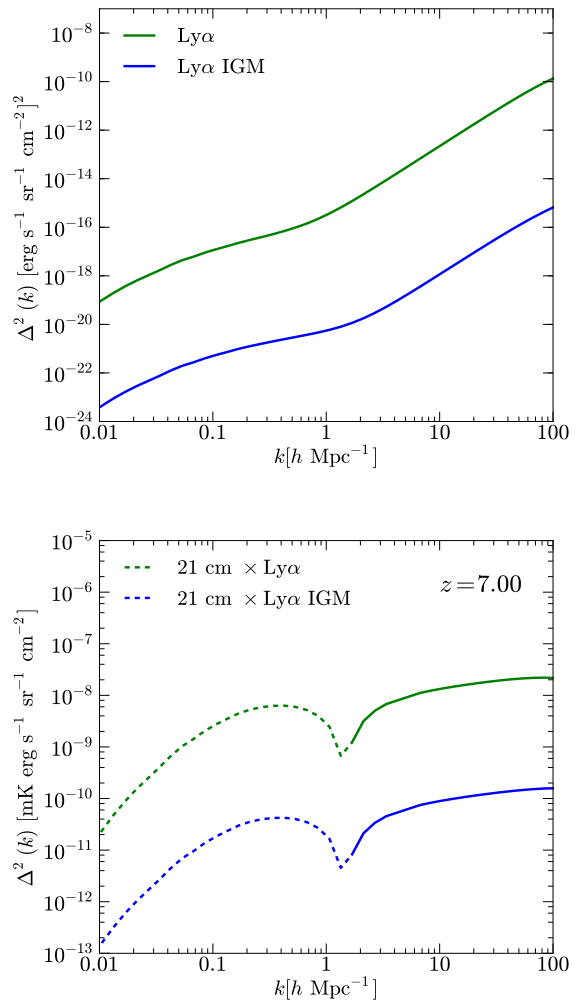


FIG. 2: IGM contribution to both the auto- and cross-power spectra at $z = 7$. The IGM component is negligible, compared to the galaxy. The dashed portion is negative. In the y axis, $\Delta^2(k) = k^3/(2\pi^2)P(k)$.

in Fourier space becomes $\mathbf{k}_{f \rightarrow s} = (\chi_s/\chi_f k_\perp, y_s/y_f k_\parallel)$, which is not radially symmetric. The low- z foregrounds are identified as H α [6563 Å, $z = 0.5$], OIII [5007 Å, $z = 0.9$], and OII [3727 Å, $z = 1.6$] with luminosities $L_{\text{H}\alpha} = 1.3 \times 10^{41} \frac{\text{SFR}}{M_\odot \text{yr}^{-1}}$, $L_{\text{OII}} = 7.1 \times 10^{40} \frac{\text{SFR}}{M_\odot \text{yr}^{-1}}$, and $L_{\text{OIII}} = 1.3 \times 10^{41} \frac{\text{SFR}}{M_\odot \text{yr}^{-1}}$, respectively. The low- z SFR is exclusively modeled as

$$\frac{\text{SFR}(M, z)}{M_\odot \text{yr}^{-1}} = 10^{a+bz} \left(\frac{M}{M_1}\right)^c \left(\frac{M}{M_2}\right)^d \quad (33)$$

for the foreground line emissions. This SFR model is fitted to the numerical simulations below $z = 2$ and the parameters are constrained as $a = -9.097$, $b = 0.484$, $c = 2.7$, $d = -4.0$, $M_1 = 10^8 M_\odot$, and $M_2 = 8 \times 10^{11} M_\odot$ [23].

The projected power spectrum of the foreground is

then expressed as

$$P_{f \rightarrow s}(k_{\perp}, k_{\parallel}, z_s) = \left(\frac{\chi_s}{\chi_f} \right)^2 \frac{y_s}{y_f} P(k_f, z_f) \quad (34)$$

and $k_f = \sqrt{(\chi_s/\chi_f)^2 k_{\perp}^2 + (y_s/y_f)^2 k_{\parallel}^2}$. In Figure 3, we show the unprojected and projected power spectra for H α . OIII and OII show similar contours so they are neglected. In Figure 4, the blue and red curves are radially averaged from the anisotropic power spectra.

In Figures 4 and 5, we show the power spectra for Ly α and the foreground lines H α , OIII, and OII with projection and with flux masking at redshifts $z = 7$ and 9. The projected foreground emissions are much higher than the Ly α lines. By selecting the brightest sources at the flux detection threshold and forming a mask, we can effectively remove those ‘‘hot’’ pixels which only account for a very tiny fraction of the sky coverage [22, 23]. As can be seen in Figure 6, we show the percentage of the removed pixels as the threshold flux changes. We find that a flux cut at 10^{-18}W/m^2 can significantly lower amplitudes of the foreground power spectra while only removing less than 0.1% of the pixels. Therefore, the flux masking procedure makes the low- z foregrounds negligible.

The synchrotron radiation dominates the 21 cm signals but its smooth spectral feature can easily be used to isolate this component in frequency domain, also the galactic foregrounds are not correlated with extragalactic line emissions at low- z . So we do not expect any noticeable cross-correlations between galactic synchrotron and Ly α foregrounds. However, the radio point sources that are too faint to be resolved are indeed correlated with the low- z foregrounds within $0.5 < z < 1.6$, so this component would be picked up in the 21 cm–Ly α cross-correlation, making it not as systematic-free as expected. To estimate its contribution, we use the model in Refs. [54–56]. The model is described as

$$\delta_{\text{radio}}(\mathbf{x}) = \left(\frac{\partial B_{\nu}}{\partial T} \right)^{-1} I_{\nu}^{\text{radio}} \delta_g(\mathbf{x}) \quad (35)$$

based on the fact that the radio point source is a tracer of underlying density field. Here we have defined $I_{\nu}^{\text{radio}} = \int_0^{S_{\text{cut}}} dS S dN/dS$ and assume a flux limit $S_{\text{cut}} = 1 \text{ mJy}$, above which the radio point sources are bright enough to be resolved. The flux distribution is a simple power-law, i.e., $dN/dS = A(S/S_0)^{\alpha}$, where $A = 4 \text{ mJy}^{-1} \text{ sr}^{-1}$, $S_0 = 880 \text{ mJy}$, and $\alpha = -1.75$ [53]. Also, $\partial B_{\nu}/\partial T = 99.27 \text{ Jy sr}^{-1}/(\mu\text{K})x^4 e^x/(e^x-1)^2$ and $x = h\nu/k_b T_{\text{CMB}} = \nu/56.84 \text{ (GHz)}$. In Fourier space, the shape functions of the halo model for the radio sources are described as

$$X_l(k, M, z) = \frac{\sqrt{2N_c N_s u(k, M, z) + N_s^2 u^2(k, M, z)}}{\bar{n}_g} \quad (36)$$

and

$$\tilde{X}_l(k, M, z) = \frac{N_s u(k, M, z)}{\bar{n}_g}, \quad (37)$$

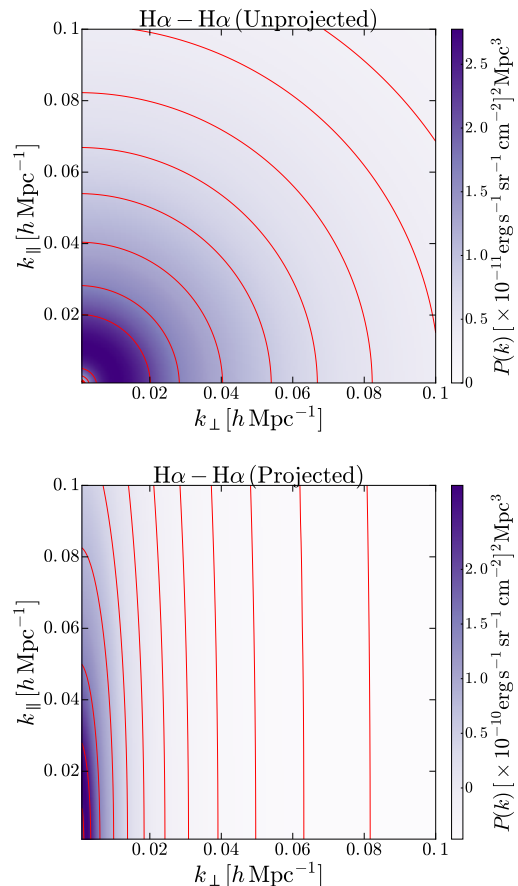


FIG. 3: Power spectrum projection of H α at $z = 7$. OIII and OII power spectrum projections have similar patterns.

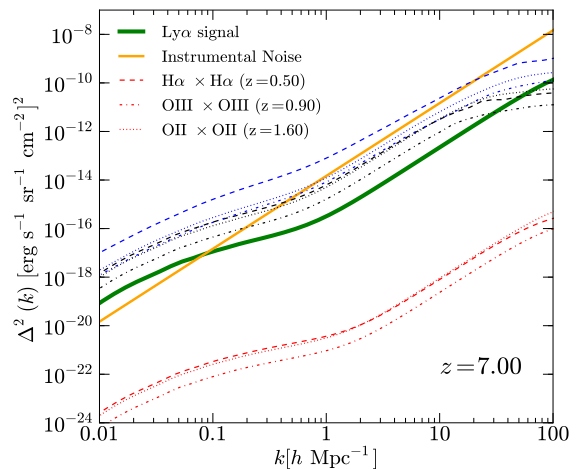


FIG. 4: Ly α power spectrum at $z = 7$ (green). We show the low- z foreground power spectra with no projection (black), projection (blue), and masking (red). The instrumental noise (orange) is derived from the proposed CDIM specification listed in Table II.

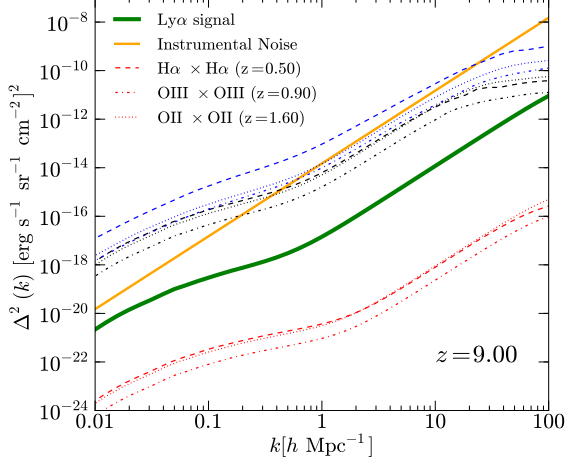


FIG. 5: Ly α power spectrum at $z = 9$ (green). The description of other lines is the same as Figure 4.

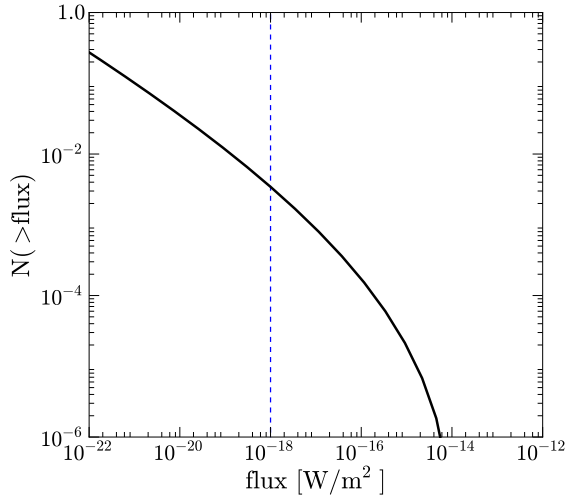


FIG. 6: Flux threshold of H α line at $z = 0.5$.

which are directly inserted into Eqs. (23) and (24) to obtain the one-halo and two-halo terms for the point-source clustering. Both $X_l(k, M, z)$ and $\tilde{X}_l(k, M, z)$ describe the Fourier-space profile of a point source with mass M located at redshift z . Here the central and satellite galaxy numbers are

$$N_c(M) = \frac{1}{2} \left[1 + \operatorname{erf} \left(\frac{\log_{10} M - \log_{10} M_{\min}}{\sigma_M} \right) \right] \quad (38)$$

and

$$N_s(M) = \frac{1}{2} \left[1 + \operatorname{erf} \left(\frac{\log_{10} M - \log_{10} 2M_{\min}}{\sigma_M} \right) \right] \left(\frac{M}{M_s} \right)^{\alpha_s}. \quad (39)$$

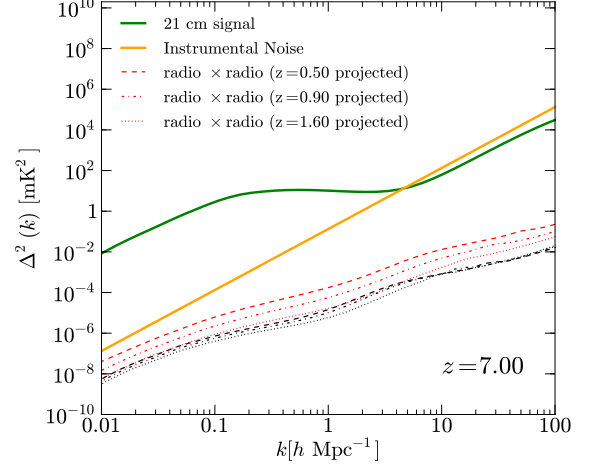


FIG. 7: 21 cm power spectrum at $z = 7$ (green). The radio flux cut is $S_{\text{cut}} = 1$ mJy. The instrumental noise (orange) is derived from the SKA specification in Table I. The low- z foreground line and its projection are shown in black and red, respectively, for each redshift when a Ly α foreground line is present. A spectral fitting scheme for the radio sources is assumed and the suppression factor is assumed to be 10^{-6} [53].

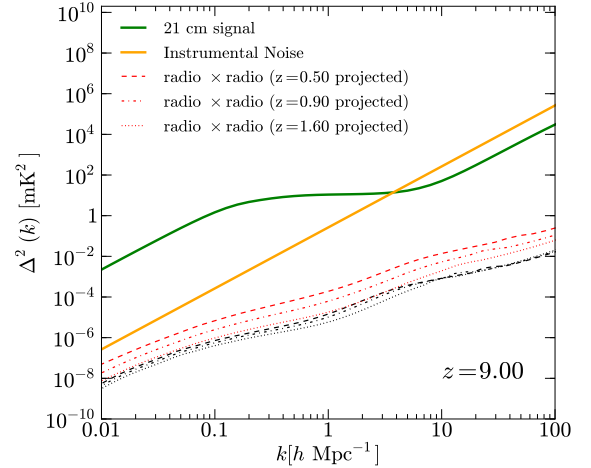


FIG. 8: 21 cm power spectrum at $z = 9$ (green). The description of other lines is the same as Figure 7.

The mean galaxy number density is

$$\bar{n}_g(z) = \int dM n(M, z) N_g(M), \quad (40)$$

where $N_g(M) = N_c(M) + N_s(M)$. The parameters determined from luminosity and color dependence of galaxy clustering in the SDSS DR7 main galaxy sample are $M_{\min} = 10^9 M_{\odot}$, $\sigma_M = 0.2$, $M_s = 5 \times 10^{10} M_{\odot}$, and $\alpha_s = 1$ [57].

We estimate that the radio foreground contributions at the Ly α foreground redshifts and the raw power spectra

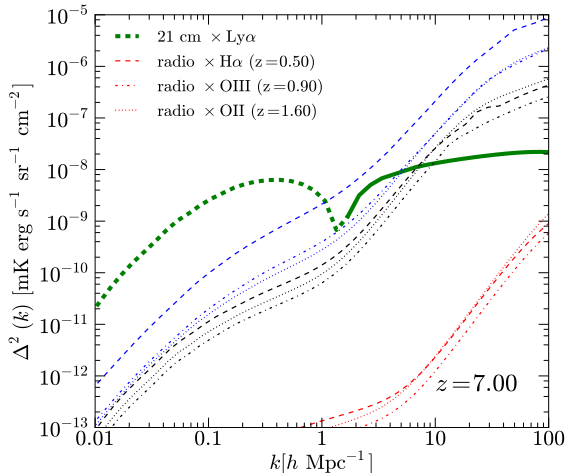


FIG. 9: 21 cm–Ly α cross-power spectrum at $z = 7$ (green); the green dashed line indicates that it is negative. We show the radio-line foreground cross-power spectra with no projection cut (black), projection (blue), and masking (red). The radio flux cut is $S_{\text{cut}} = 1$ mJy. The instrumental noise for the cross-correlation is zero.

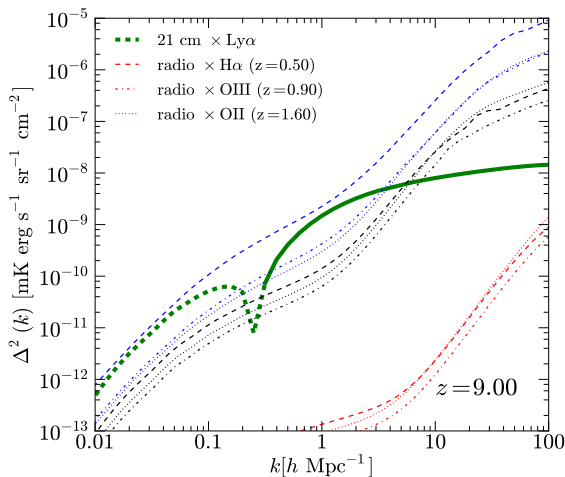


FIG. 10: 21 cm–Ly α cross-power spectrum at $z = 9$ (green). The description of other lines is the same as Figure 9.

are a few orders of magnitude higher than the 21 cm signal as revealed by [53, 58]. Therefore, the foreground suppression is very crucial; the spectral fitting procedure studied in [53] demonstrated that the radio foregrounds can be reduced by six orders of magnitude in map space, and it has been validated that this is true from flux cut 0.1–100 mJy. Consequently, the radio foreground contamination becomes negligible, and we show all of the power spectra in Figures 7 and 8 at redshifts $z = 7$ and 9. We see that the resulting radio point sources have very negligible contaminating power on the

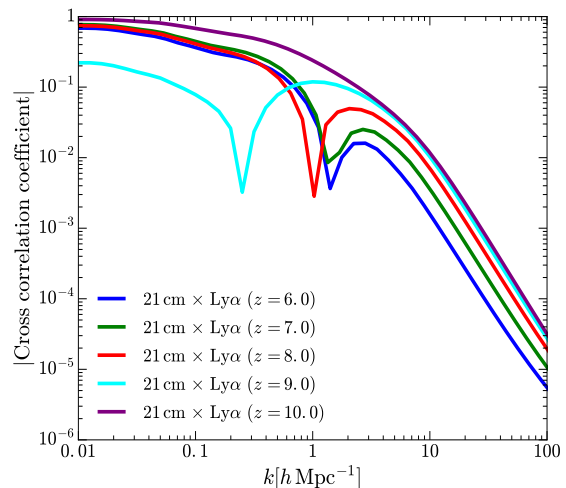
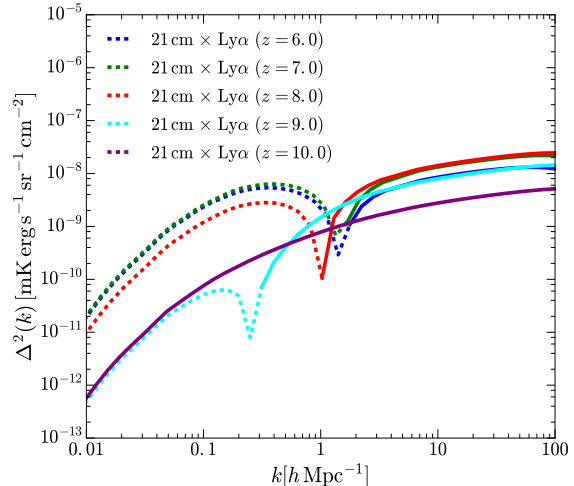


FIG. 11: Top: redshift evolution of the 21 cm–Ly α cross-correlation as a function of k . The mean ionization fractions are $\bar{x}_{\text{H}} = 0.94$ ($z = 6$), $\bar{x}_{\text{H}} = 0.80$ ($z = 7$), $\bar{x}_{\text{H}} = 0.48$ ($z = 8$), $\bar{x}_{\text{H}} = 0.16$ ($z = 9$), and $\bar{x}_{\text{H}} = 0.04$ ($z = 10$). Bottom: cross-correlation coefficient as a function of k at different redshifts.

21 cm measurements. Finally, we show the 21 cm–Ly α cross-power spectra at redshifts $z = 7$ and 9 in Figures 9 and 10 with both foreground separation schemes incorporated. In Figure 11, we show both the evolutions and cross-correlation coefficients of the 21 cm–Ly α cross-power spectrum as a function of k from $z = 6$ to $z = 10$.

Despite the fact that all of the foreground cross-correlations are small, this has to rely on the assumption that we have very efficient foreground mitigation strategies for both 21 cm and Ly α measurements. Non-negligible foreground residuals on 21 cm and Ly α would make a great impact on the power spectrum uncertainties, even if they are uncorrelated.

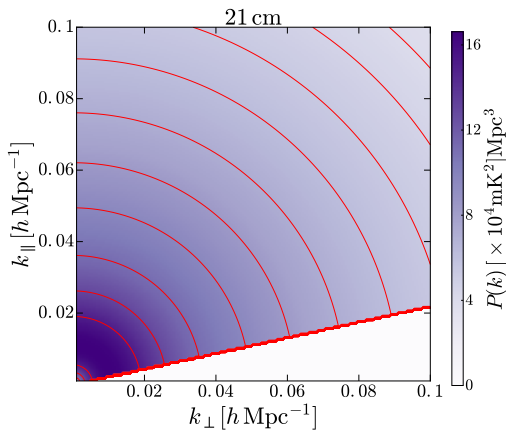


FIG. 12: 2D power spectrum of 21 cm at $z = 7$ with foreground wedge.

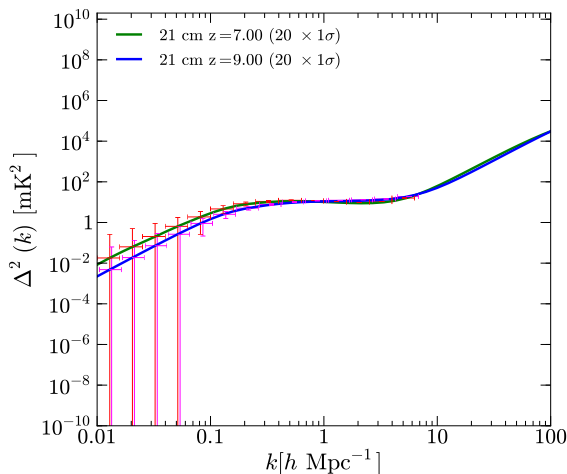


FIG. 13: Forecast 21 cm power spectra at $z = 7$ and 9 for experiment SKA. The multiplicative numbers in parentheses enlarge the error bars for visualization purposes.

V. FORECAST FOR THE EXPERIMENTS

In this section, we consider two experiments, SKA and Cosmic Dawn Intensity Mapper (CDIM) [59, 60], and investigate the detectability of the 21 cm–Ly α cross-correlation with both instrumental noises and foregrounds. We list the experimental specifications in Tables I and II.

The instrumental noise of the 21 cm experiment is entirely determined by some key factors such as integration time t_0 , system temperature T_{sys} , maximum baseline D_{max} , collecting area A_{tot} , antenna number N_a , and frequency resolution $d\nu$. The noise is then given by

$$P_N^{21 \text{ cm}} = \chi^2 y \pi \left(\frac{\lambda D_{\text{max}} T_{\text{sys}}}{A_{\text{tot}} N_a} \right)^2 \frac{1}{t_0}. \quad (41)$$

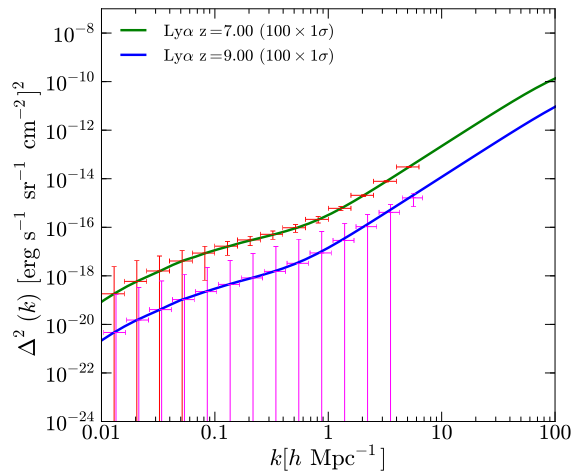


FIG. 14: Forecast Ly α power spectra at $z = 7$ and 9 for experiment CDIM. The multiplicative numbers in parentheses enlarge the error bars for visualization purposes.

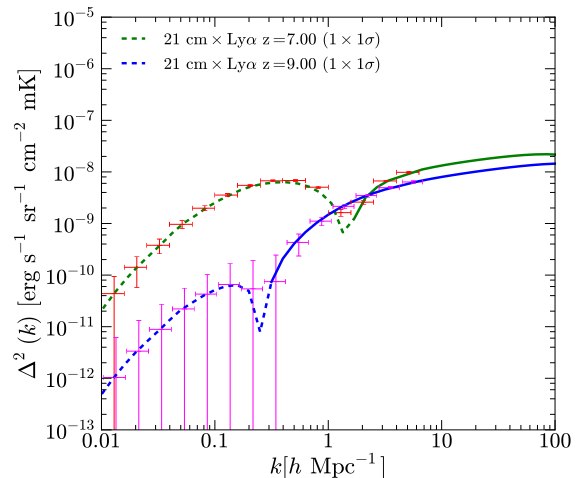


FIG. 15: Forecast 21 cm–Ly α cross-power spectra at $z = 7$ and 9 for experiments SKA and CDIM. The multiplicative numbers in parentheses enlarge the error bars for visualization purposes.

For the Ly α experiments, the noise is

$$P_N^{\text{Ly}\alpha} = V_{\text{pix}} \sigma_N^2, \quad (42)$$

where the comoving volume subtended by the detector pixel

$$V_{\text{pix}} = \chi^2 A_{\text{pix}} y \delta_\nu \quad (43)$$

depends on the pixel area A_{pix} and frequency resolution δ_ν . The general Knox formula [61] for the measured sig-

TABLE I: 21 cm Experiment

Exp.	λ^{rest} (m)	D_{max} (m)	T_{sys} (K)	t_0 (hr)	A_{tot} (m ²)	FOV (deg ²)	BW	$\delta\nu$	N_a	z
SKA1-LOW	0.21	1000	400	1000	925	13	18MHz	3.9kHz	433	8

TABLE II: Ly α Experiment

Exp.	λ^{rest} (Å)	Ω_{pix} (")	A_s (deg ²)	σ_{pix} (erg s ⁻¹ cm ⁻² sr ⁻¹)	$\lambda/\delta\lambda$	BW (μm)
CDIM	1216	1	300	3×10^{-6}	500	0.7-8.0

nal 21 cm or Ly α is

$$\Delta P_{X,Y}(k, z) = \sqrt{\frac{\tilde{P}_{X,Y}^2(k, z) + \tilde{P}_{XX}(k, z)\tilde{P}_{YY}(k, z)}{N_m}}, \quad (44)$$

and the number of modes in the bin k is $N_m = 2\pi k^2 \Delta k \frac{V_s}{(2\pi)^3}$. Here $X, Y = \{21 \text{ cm}, \text{Ly}\alpha\}$, the survey volume is $V_s = \chi^2 A_s y B_\nu$, A_s is the survey area, and B_ν is the bandwidth (BW). For Ly α experiments, the minimum and maximum scales are determined by the survey and pixel areas. For 21 cm, we normally consider modes at scales below $k = 10 \text{ Mpc}^{-1}$ and get the minimum k from the total survey area. For the cross-correlation, the common k range is chosen from two experiments and the minimum volume between the 21 cm and Ly α experiments is taken to calculate the number of modes. The noise- and foreground-included power spectra are formed as $\tilde{P}_{21 \text{ cm}} = P_{21 \text{ cm}} + P_{21 \text{ cm}}^N + P_{21 \text{ cm}}^{\text{radio}}$, $\tilde{P}_{\text{Ly}\alpha} = P_{\text{Ly}\alpha} + P_{\text{Ly}\alpha}^N + P_{\text{Ly}\alpha}^{\text{low-}z}$, and $\tilde{P}_{21 \text{ cm-Ly}\alpha} = P_{21 \text{ cm-Ly}\alpha} + P_{21 \text{ cm-Ly}\alpha}^{\text{radio-low-}z}$. The k region is binned in log-space and we calculate the errors using Eq. (44) for each k -band.

Following Ref. [62], we also consider the foreground wedge in Fourier space and its impact on the power spectrum sensitivity. For SKA, the characteristic angle θ_0 is chosen to be $\sqrt{\text{FOV}} \sim 4^\circ$. The wedge cut reduces the effective modes N_m in Fourier space and decreases the overall signal-to-noise by 8%, which could be much larger if a bigger angle θ_0 is assumed. In Figure 12, we show the reduced region by the foreground wedge using a 2D 21 cm power spectrum. In addition to the modes cut by the wedge, low k_{\parallel} modes are strongly contaminated by foreground and should be excluded as well. A large k_{max} can compensate for the loss of modes due to the horizontal cut. For example, at $k_{\text{max}} = 10 \text{ hMpc}^{-1}$, a horizontal cut between $0.05 \text{ hMpc}^{-1} < k_{\parallel} < 0.1 \text{ hMpc}^{-1}$ introduces negligible changes to the overall signal-to-noise. But for a small k_{max} , such as 0.5 hMpc^{-1} , the total wedge could reduce the signal-to-noise by 11% with a horizontal cut at $k_{\parallel} = 0.1 \text{ hMpc}^{-1}$.

In Figures 13, 14 and 15, we show all of the power spectra and their band errors for 21 cm and Ly α at $z = 7$ and 9. As can be seen from Figure 15, the anti-correlations between neutral hydrogen and galaxies can be probed at very high signal-to-noise ratios.

From the forecasted power spectra in Figure 15, we can further try to constrain the EoR parameters defined as $\mathbf{P} = \{\tau, \Delta y, \sigma_{\ln R}\} = \{0.058, 6.0, 1.0\}$. The Fisher matrix [63] is

$$F_{ij} = \sum_{k,z} \frac{1}{(\Delta\eta(k, z))^2} \frac{\partial\Delta^2(k, z)}{\partial p_i} \frac{\partial\Delta^2(k, z)}{\partial p_j}. \quad (45)$$

Here $\Delta\eta(k, z)$ is the error on the cross-power spectrum Δ^2 and p_i refers to any parameters in the set \mathbf{P} and $\Delta^2 = k^3/(2\pi^2)P_{21 \text{ cm-Ly}\alpha}$. All of the 1σ confidence levels, as well as the likelihood functions in Figure 16, are calculated from the 21 cm–Ly α cross-power spectra at $z = 7$ and 9. As can be seen in the figure, the bubble size can be constrained from the cross-correlation while the errors on the optical depth and duration of the reionization transition are large. This is due to the fact that the cross-correlation is proportional to $x_e(z)$ and not $x_e^2(z)$, to which the 21 cm–21 cm and 21 cm– τ [38] are proportional. Therefore, the cross-power spectrum at a single redshift is less sensitive to the reionization history. However, the cross-correlations at different redshifts might be able to break the degeneracies among the parameters, and so are useful as complementary probes to cosmological and astrophysical problems. In Figure 17, we reduce the bandwidth by a factor of 5 and combine the cross-power spectra measured at $z = 6, 7, 8, 9$, and 10. It is seen that the Fisher matrix error bars on all of the parameters are significantly reduced, and that multi-redshift measurements within narrow bins can effectively break the parameter degeneracies.

VI. CONCLUSION

In this work, we applied a bubble model to the computation of 21 cm and Ly α cross-correlation at the EoR. Making use of the empirical relation between Ly α luminosity and mass for the line emissions, we also calculated the power spectra for Ly α . The 21 cm–Ly α cross-power spectrum in this fast approach can reproduce the key features of the one made by detailed numerical simulations, and we can use it to quickly assess the overall performance of the future EoR experiments.

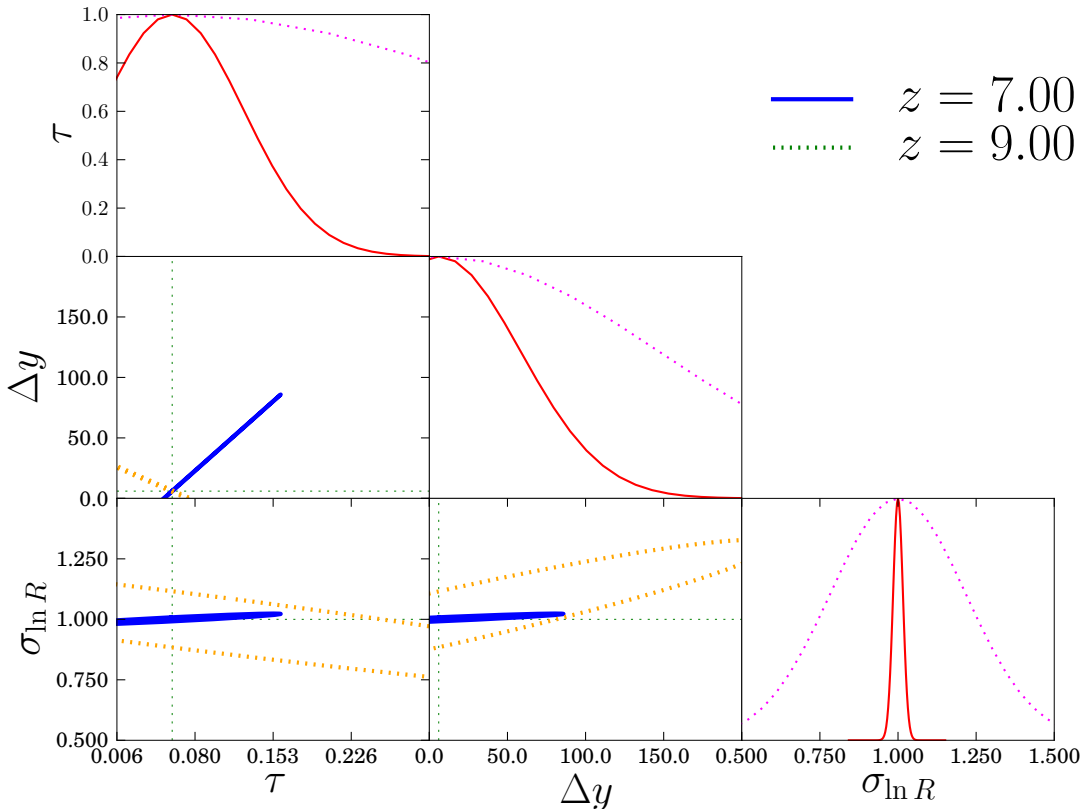


FIG. 16: $1\text{-}\sigma$ confidence levels for the optical depth τ , the EoR duration Δy , and the rms of the bubble size $\sigma_{\ln R}$ at $z = 7$ (solid, $\bar{x}_H = 0.80$) and 9 (dotted, $\bar{x}_H = 0.16$).

The cross-correlation is contaminated by the low- z foregrounds for both 21 cm and $\text{Ly}\alpha$. We studied the radio galaxies for the 21 cm experiments and $\text{H}\alpha$, OIII, and OII line emissions for the $\text{Ly}\alpha$ experiments. All of these foregrounds could be a few orders of magnitude higher than the signals we are probing if the foreground mitigation is not incorporated. The map-space spectral fitting can effectively remove the radio point-source contaminations, while a flux masking for the intensity mapping experiments have been shown to be a good and easy

foreground-removal method.

We take advantage of this efficient algorithm and estimate the errors on the EoR parameters τ , Δy and $\sigma_{\ln R}$, based on the Fisher matrix formalism. For other physical processes during the EoR, such as X-ray heating, supernovae explosion, and shock heating, numerical simulations with these effects or an extension to this work should be devised. We will discuss these in the future works.

-
- [1] A. Loeb and R. Barkana, *Annu. Rev. Astron. Astrophys.* **39**, 19 (2001), astro-ph/0010467.
- [2] M. McQuinn, S. R. Furlanetto, L. Hernquist, O. Zahn, and M. Zaldarriaga, *Astrophys. J.* **630**, 643 (2005), astro-ph/0504189.
- [3] D. R. G. Schleicher, R. Banerjee, and R. S. Klessen, *Astrophys. J.* **692**, 236 (2009), 0808.1461.
- [4] S. R. Furlanetto, S. P. Oh, and E. Pierpaoli, *Phys. Rev. D* **74**, 103502 (2006), astro-ph/0608385.
- [5] X. Fan, C. L. Carilli, and B. Keating, *Annu. Rev. Astron. Astrophys.* **44**, 415 (2006), astro-ph/0602375.
- [6] A. Konno, M. Ouchi, Y. Ono, K. Shimasaku, T. Shibuya, H. Furusawa, K. Nakajima, Y. Naito, R. Momose, S. Yuma, et al., *Astrophys. J.* **797**, 16 (2014), 1404.6066.
- [7] S. Malhotra and J. E. Rhoads, *Astrophys. J.* **617**, L5 (2004), astro-ph/0407408.
- [8] S. Malhotra and J. E. Rhoads, *Astrophys. J.* **647**, L95 (2006), astro-ph/0511196.
- [9] E. Komatsu, K. M. Smith, J. Dunkley, C. L. Bennett, B. Gold, G. Hinshaw, N. Jarosik, D. Larson, M. R. Nolte, L. Page, et al., *Astrophys. J. Suppl. Ser.* **192**, 18 (2011), 1001.4538.

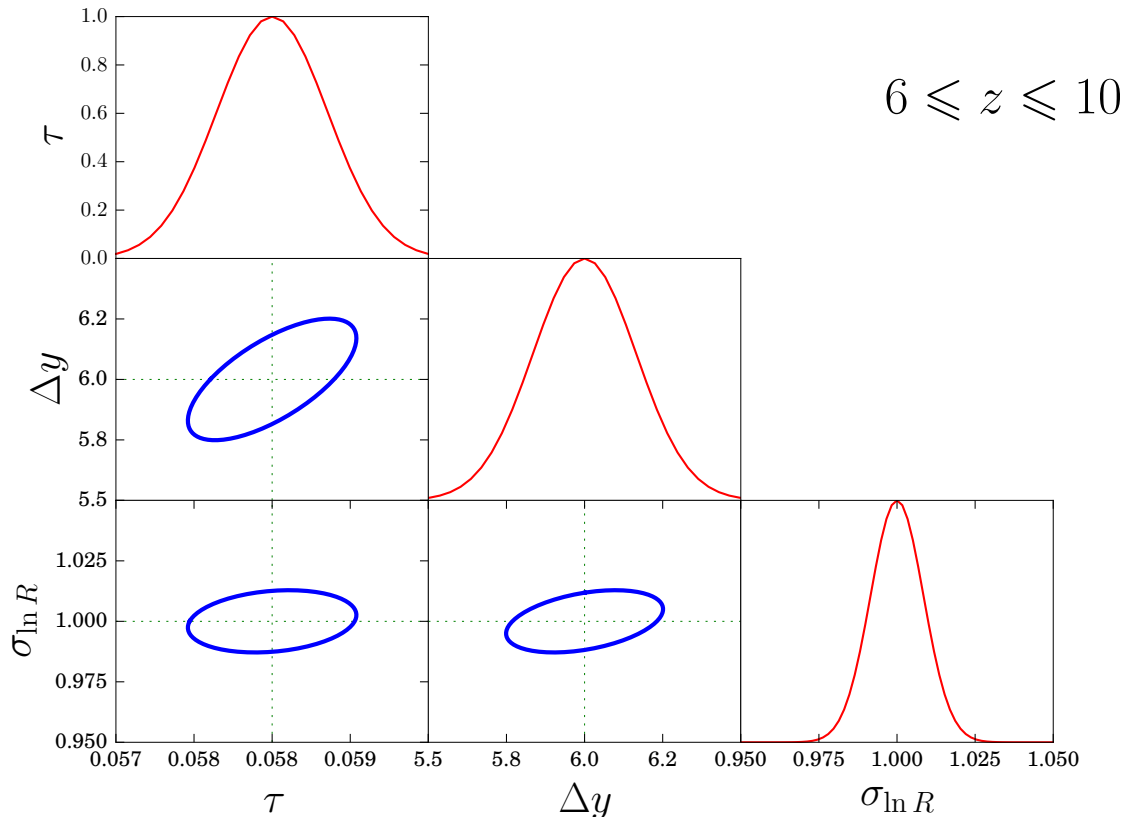


FIG. 17: $1\text{-}\sigma$ confidence levels for the optical depth τ , the EoR duration Δy , and the rms of the bubble size $\sigma_{\ln R}$ at $6 \leq z \leq 10$.

- [10] Planck Collaboration, R. Adam, N. Aghanim, M. Ashdown, J. Aumont, C. Baccigalupi, M. Ballardini, A. J. Banday, R. B. Barreiro, N. Bartolo, et al., *Astron. Astrophys.* **596**, A108 (2016), 1605.03507.
- [11] M. P. van Haarlem, M. W. Wise, A. W. Gunst, G. Heald, J. P. McKean, J. W. T. Hessels, A. G. de Bruyn, R. Nijboer, J. Swinbank, R. Fallows, et al., *Astron. Astrophys.* **556**, A2 (2013), 1305.3550.
- [12] S. J. Tingay, R. Goeke, J. D. Bowman, D. Emrich, S. M. Ord, D. A. Mitchell, M. F. Morales, T. Booler, B. Crosse, R. B. Wayth, et al., *Publ. Astron. Soc. Aust.* **30**, e007 (2013), 1206.6945.
- [13] A. R. Parsons, D. C. Backer, G. S. Foster, M. C. H. Wright, R. F. Bradley, N. E. Gugliucci, C. R. Parashare, E. E. Benoit, J. E. Aguirre, D. C. Jacobs, et al., *Astron. J.* **139**, 1468 (2010), 0904.2334.
- [14] D. R. DeBoer, A. R. Parsons, J. E. Aguirre, P. Alexander, Z. S. Ali, A. P. Beardsley, G. Bernardi, J. D. Bowman, R. F. Bradley, C. L. Carilli, et al., *ArXiv e-prints* (2016), 1606.07473.
- [15] L. Koopmans, J. Pritchard, G. Mellema, J. Aguirre, K. Ahn, R. Barkana, I. van Bemmell, G. Bernardi, A. Bonaldi, F. Briggs, et al., *Advancing Astrophysics with the Square Kilometre Array (AASKA14) 1* (2015), 1505.07568.
- [16] S. R. Furlanetto, S. P. Oh, and F. H. Briggs, *Phys. Rep.* **433**, 181 (2006), astro-ph/0608032.
- [17] A. Bonaldi and M. L. Brown, *Mon. Not. R. Astron. Soc.* **447**, 1973 (2015), 1409.5300.
- [18] A. Liu, M. Tegmark, and M. Zaldarriaga, *Mon. Not. R. Astron. Soc.* **394**, 1575 (2009), 0807.3952.
- [19] A. Mesinger, S. Furlanetto, and R. Cen, *Mon. Not. R. Astron. Soc.* **411**, 955 (2011), 1003.3878.
- [20] Z. S. Ali, A. R. Parsons, H. Zheng, J. C. Pober, A. Liu, J. E. Aguirre, R. F. Bradley, G. Bernardi, C. L. Carilli, C. Cheng, et al., *Astrophys. J.* **809**, 61 (2015), 1502.06016.
- [21] H. Jensen, P. Laursen, G. Mellema, I. T. Iliev, J. Sommer-Larsen, and P. R. Shapiro, *Mon. Not. R. Astron. Soc.* **428**, 1366 (2013), 1206.4028.
- [22] A. R. Pullen, O. Doré, and J. Bock, *Astrophys. J.* **786**, 111 (2014), 1309.2295.
- [23] Y. Gong, M. Silva, A. Cooray, and M. G. Santos, *Astrophys. J.* **785**, 72 (2014), 1312.2035.
- [24] S. R. Furlanetto and A. Lidz, *Astrophys. J.* **660**, 1030 (2007), astro-ph/0611274.
- [25] A. Lidz, O. Zahn, S. R. Furlanetto, M. McQuinn, L. Hernquist, and M. Zaldarriaga, *Astrophys. J.* **690**, 252 (2009), 0806.1055.
- [26] J. S. B. Wyithe and A. Loeb, *Mon. Not. R. Astron. Soc.* **375**, 1034 (2007), astro-ph/0609734.
- [27] D. Vrbancic, B. Ciardi, V. Jelić, H. Jensen, S. Zaroubi, E. R. Fernandez, A. Ghosh, I. T. Iliev, K. Kakiichi, L. V. E. Koopmans, et al., *Mon. Not. R. Astron. Soc.*

- 457**, 666 (2016), 1509.03464.
- [28] A. Lidz, S. R. Furlanetto, S. P. Oh, J. Aguirre, T.-C. Chang, O. Doré, and J. R. Pritchard, *Astrophys. J.* **741**, 70 (2011), 1104.4800.
- [29] V. Jelić, S. Zaroubi, N. Aghanim, M. Douspis, L. V. E. Koopmans, M. Langer, G. Mellema, H. Tashiro, and R. M. Thomas, *Mon. Not. R. Astron. Soc.* **402**, 2279 (2010), 0907.5179.
- [30] I. T. Iliev, G. Mellema, U.-L. Pen, H. Merz, P. R. Shapiro, and M. A. Alvarez, *Mon. Not. R. Astron. Soc.* **369**, 1625 (2006), astro-ph/0512187.
- [31] I. Iliev, M. Santos, A. Mesinger, S. Majumdar, and G. Mellema, *Advancing Astrophysics with the Square Kilometre Array (AASKA14)* **7** (2015), 1501.04213.
- [32] O. Zahn, A. Lidz, M. McQuinn, S. Dutta, L. Hernquist, M. Zaldarriaga, and S. R. Furlanetto, *Astrophys. J.* **654**, 12 (2007), astro-ph/0604177.
- [33] O. Zahn, A. Mesinger, M. McQuinn, H. Trac, R. Cen, and L. E. Hernquist, *Mon. Not. R. Astron. Soc.* **414**, 727 (2011), 1003.3455.
- [34] A. Mesinger and S. Furlanetto, *Astrophys. J.* **669**, 663 (2007), 0704.0946.
- [35] M. G. Santos, L. Ferramacho, M. B. Silva, A. Amblard, and A. Cooray, *Mon. Not. R. Astron. Soc.* **406**, 2421 (2010), 0911.2219.
- [36] S. R. Furlanetto, M. Zaldarriaga, and L. Hernquist, *Astrophys. J.* **613**, 1 (2004), astro-ph/0403697.
- [37] A. Lewis, *Phys. Rev. D* **78**, 023002 (2008), 0804.3865.
- [38] P. D. Meerburg, C. Dvorkin, and D. N. Spergel, *Astrophys. J.* **779**, 124 (2013), 1303.3887.
- [39] Y. Gong, A. Cooray, M. B. Silva, M. G. Santos, and P. Lubin, *Astrophys. J.* **728**, L46 (2011), 1101.2892.
- [40] M. Zaldarriaga, S. R. Furlanetto, and L. Hernquist, *Astrophys. J.* **608**, 622 (2004), astro-ph/0311514.
- [41] S. R. Furlanetto, M. Zaldarriaga, and L. Hernquist, *Astrophys. J.* **613**, 1 (2004), astro-ph/0403697.
- [42] A. Lidz, O. Zahn, M. McQuinn, M. Zaldarriaga, S. Dutta, and L. Hernquist, *Astrophys. J.* **659**, 865 (2007), astro-ph/0610054.
- [43] R. M. Thomas and S. Zaroubi, *Mon. Not. R. Astron. Soc.* **410**, 1377 (2011), 1009.5441.
- [44] J. F. Navarro, C. S. Frenk, and S. D. M. White, *Astrophys. J.* **462**, 563 (1996), astro-ph/9508025.
- [45] C. Feng, A. Cooray, and B. Keating, *ArXiv e-prints* (2016), 1608.04351.
- [46] M. J. Mortonson and W. Hu, *Astrophys. J.* **657**, 1 (2007), astro-ph/0607652.
- [47] X. Wang and W. Hu, *Astrophys. J.* **643**, 585 (2006), astro-ph/0511141.
- [48] M. B. Silva, M. G. Santos, Y. Gong, A. Cooray, and J. Bock, *Astrophys. J.* **763**, 132 (2013), 1205.1493.
- [49] Z. Zheng, R. Cen, H. Trac, and J. Miralda-Escudé, *Astrophys. J.* **716**, 574 (2010), 0910.2712.
- [50] Z. Zheng, R. Cen, H. Trac, and J. Miralda-Escudé, *Astrophys. J.* **726**, 38 (2011), 1003.4990.
- [51] J. Miralda-Escudé, *Astrophys. J.* **501**, 15 (1998), astro-ph/9708253.
- [52] M. B. Silva, R. Kooistra, and S. Zaroubi, *Mon. Not. R. Astron. Soc.* **462**, 1961 (2016), 1603.06952.
- [53] A. Liu, M. Tegmark, and M. Zaldarriaga, *Mon. Not. R. Astron. Soc.* **394**, 1575 (2009), 0807.3952.
- [54] L. Glezer, A. Nusser, and A. J. Benson, *Mon. Not. R. Astron. Soc.* **391**, 383 (2008), 0712.0497.
- [55] J. Singal, L. Stawarz, A. Lawrence, and V. Petrosian, *Mon. Not. R. Astron. Soc.* **409**, 1172 (2010), 0909.1997.
- [56] P. Serra, A. Cooray, A. Amblard, L. Pagano, and A. Melchiorri, *Phys. Rev. D* **78**, 043004 (2008), 0806.1742.
- [57] I. Zehavi, Z. Zheng, D. H. Weinberg, M. R. Blanton, N. A. Bahcall, A. A. Berlind, J. Brinkmann, J. A. Frieman, J. E. Gunn, R. H. Lupton, et al., *Astrophys. J.* **736**, 59 (2011), 1005.2413.
- [58] D. Alonso, P. G. Ferreira, and M. G. Santos, *Mon. Not. R. Astron. Soc.* **444**, 3183 (2014), 1405.1751.
- [59] J. Pritchard, K. Ichiki, A. Mesinger, R. B. Metcalf, A. Pourtsidou, M. Santos, F. B. Abdalla, T. C. Chang, X. Chen, J. Weller, et al., *Advancing Astrophysics with the Square Kilometre Array (AASKA14)* **12** (2015), 1501.04291.
- [60] A. Cooray, J. Bock, D. Burgarella, R. Chary, T.-C. Chang, O. Doré, G. Fazio, A. Ferrara, Y. Gong, M. Santos, et al., *ArXiv e-prints* (2016), 1602.05178.
- [61] J. D. Bowman, M. F. Morales, and J. N. Hewitt, *Astrophys. J.* **638**, 20 (2006), astro-ph/0507357.
- [62] J. S. Dillon, A. Liu, C. L. Williams, J. N. Hewitt, M. Tegmark, E. H. Morgan, A. M. Levine, M. F. Morales, S. J. Tingay, G. Bernardi, et al., *Phys. Rev. D* **89**, 023002 (2014), 1304.4229.
- [63] J. C. Pober, A. Liu, J. S. Dillon, J. E. Aguirre, J. D. Bowman, R. F. Bradley, C. L. Carilli, D. R. DeBoer, J. N. Hewitt, D. C. Jacobs, et al., *Astrophys. J.* **782**, 66 (2014), 1310.7031.

VII. ACKNOWLEDGEMENTS

A.C. and C.F. acknowledge support from NASA grants NASA NNX16AJ69G, NASA NNX16AF39G and Ax Foundation for Cosmology at UC San Diego.